

Passive mm-wave imaging from UAVs using aperture synthesis

A. R. Harvey

School of Engineering and Physical Sciences,
Heriot Watt University, Edinburgh, UK

R. Appleby

QinetiQ
Malvern, UK

ABSTRACT

Passive imaging using mm-waves offers very significant advantages in scientific and military surveillance. However, the relatively long wavelengths mean that for the resolutions that are typically sought, the input aperture of the imager needs to be quite large; typically in excess of one metre. Deployment of conventional dish antennae of these dimensions on small aircraft is highly problematic. The use of snapshot synthetic aperture interferometric radiometry (SAIR) offers an attractive route to integrating a two-dimensional antenna array into the structure of an aircraft so that the transverse effective dimensions of the antenna can be almost as large as the aircraft. We report here a study into the feasibility of deployment of a SAIR on unmanned airborne vehicles and the achievable performance parameters. Critical considerations are the achievement of acceptable sensitivity and angular resolution from a SAIR that does not require excessive complexity. It is shown that traditional approaches based on fully sampling the spatial frequencies in the scene are unable to simultaneously meet all of these criteria, but that a SAIR based on thinned sampling of the spatial frequencies shows promise.

NOMENCLATURE

c	speed of light
D	width of aperture
B	radiometer bandwidth
h	UAV height
K	Kelvin
n	number of antennae
nm	nanometre
N	number of sample points in support region, number of complex correlators

r_i	redundancy of baseline i
T_B	background temperature
T_A	antenna noise temperature
v	UAV speed
w	value of weighting function applied to measured visibilities
\bar{r}	average redundancy in baseline vectors
θ_x, θ_y	angular resolutions in direction cosine space
ΔT	radiometric resolution
$\Delta x, \Delta y$	antenna spacings in across-track and along-track dimensions in units of $\lambda/2$
α	angle with respect to boresight
μ_x, μ_y	across-track and along-track direction cosines
τ	integration time
λ	wavelength

1.0 INTRODUCTION

During recent conflicts in Kosovo there was 50% cloud cover for 70% of the time⁽¹⁾. This denied the effective use of visible-band and infrared sensors for a large fraction of the time. Passive mm-wave imaging (PMI) is a potential solution to this surveillance problem. Research at QinetiQ Malvern and elsewhere has shown that passive mm-wave imaging can form high contrast, natural imagery even through foul weather. This arises principally because the relatively long wavelength of mm-waves enables penetration of foul weather and obscurants such as cloud, fog, dust and smoke. Like thermal imaging, millimetre-wave imaging employs the detection of thermal emissions from the scene and so both day and night operation is possible. Differences between day and night imagery that can be observed in thermal images are not generally significant in millimetre-wave images.



Figure 1. Passive mm-wave image looking east from the Malvern Hills illustrating the natural imagery provided by passive mm-wave imaging.

An example passive mm-wave image recorded using the QinetiQ MITRE scanned passive mm-wave imager, shown in Fig. 1, is illustrative of the quality of aerial images that could be demonstrated by PMI from a UAV. Image features are due to changes in both temperature and emissivity and result in images that are easily interpreted. At these wavelengths thin layers of paint are effectively transparent so that painted metallic surfaces act as mirrors and have apparent temperatures equal to those of the scene that is reflected. In many cases, particularly when viewed from the air, the cold sky is reflected, which in the 80-90GHz band, has a characteristic temperature of about 80K in fine weather giving a contrast of about 200K with ambient background features. This contrast is some two orders of magnitude higher than readily achievable receiver sensitivities enabling high signal-to-noise ratio detection of metallic sources. Non-metallic objects, such as buildings, roads and water exhibit contrasts of a few tens of Kelvin and are also detectable with good signal-to-noise ratios.

Scientific applications of passive mm-wave imaging include aerial and space-based remote sensing of geophysical features, such as measurement and classification of snow and ice cover⁽²⁾, sea and land surface temperatures, sea surface salinity, soil moisture content and wind velocity⁽³⁾. For military applications, passive mm-wave imaging (PMI) has now reached the level of maturity where systems have been demonstrated for real-time imaging for helicopter collision avoidance (using a mechanically scanned linear focal plane array)⁽⁴⁾ and for aircraft landing (using a fully staring focal plane array)⁽⁵⁾. However, the long wavelength of mm-waves means that relatively large antennae are necessary. The resolutions required for these particular applications are of the order of 10 milliradians and can be achieved using antenna apertures of approximately 0.3m and these can be conveniently mounted into larger air platforms without compromising aircraft functionality. Radiometric sensitivities of about 1K are demonstrated and this is adequate for both flying-aid and low-resolution surveillance applications. Aerial surveillance, however, generally requires higher angular resolutions and hence larger antenna apertures and imaging-forming volumes are required. Although large aircraft may be able to accommodate the larger antennae required for PMI surveillance, its deployment on a UAV is severely restricted by the restricted payload area and volume available. For high-resolution PMI from small aircraft such as UAVs the use of synthetic apertures is the only tractable solution. By conformally integrating an antenna array into the fuselage of a UAV, it is feasible to synthesise an antenna with dimensions comparable to that of the aircraft, thus offering a route to

PMI with sub-milliradian angular resolution. We address here the design of a thinned-array synthetic aperture interferometric radiometer (SAIR) for imaging from small aerial platforms such as unmanned airborne vehicles (UAVs).

Passive synthetic aperture imaging radiometry, as discussed here, naturally invites comparison with synthetic aperture radar (SAR). SAR has been developed for all-weather, high-resolution aerial surveillance to overcome the limited resolution obtainable from small antennae. Whereas the dimensions of the airframe fundamentally limit the angular resolution for SAIR this is not true for SAR. For example, TESAR (tactical endurance synthetic aperture radar) mounted to the Predator UAV can give ground resolutions down to 0.3m where a SAIR system mounted to a Predator UAV flying at 6,000m would have a resolution limited by the maximum dimensions of the airframe to ground resolutions of about 2.5m. Clearly, to be of practical use for imaging from UAVs passive mm-wave imaging must offer complementary capabilities to SAR. Fortunately it is in the very areas where exploitation of SAR is problematic that passive mm-wave SAIR is most useful. For example, SAR cannot operate close to nadir and the shadowing associated with stand-off operation means that SAR is of limited use in urban and forested environments, whereas passive mm-wave SAIR yields its highest resolutions and contrast for nadir operation. This enables imaging with modest resolution into regions inaccessible by SAR. In addition, whereas the coherent nature of SAR results in high levels of speckle that can mask features and make images difficult to interpret, passive mm-wave images, being formed from incoherent radiation, have no speckle and a natural appearance that is easily interpreted by untrained users.

The fundamental principles of aperture synthesis radiometry were developed in the early twentieth century by optical and radio astronomers, who used several days of observing time to form a single image. Recently the techniques have been further developed by the Earth observation community with an emphasis on 'snapshot' imaging in which a single image is formed from a single observation^(6,7). Snapshot aperture synthesis offers potential for deploying the required large apertures in Earth orbit without the large mass associated with conventional dishes. In addition, the optical aberrations that limit the field of view of dish antennae are absent, so swath widths are theoretically limited only by the reduced resolution caused by foreshortening of the antenna aperture.

Although a large filled aperture could be synthesised with a SAIR system by completely filling the aperture with receiving antennae,

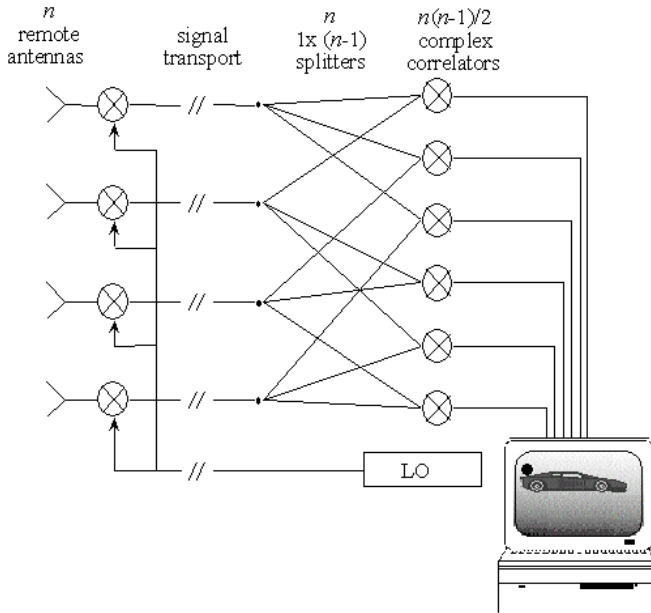


Figure 2. Schematic of the essential components of a synthetic aperture imaging radiometer.

this is not useful and is not necessary. A carefully designed sparse array of antennae can achieve an equivalent point spread function or impulse response to that of a filled dish, but with considerably reduced complexity and mass; a sparse array SAIR employing an array of n antennae enables the formation of an image containing n^2 pixels, whereas a filled aperture yielding the same pixel count would require n^2 antennae. For this reason, filled synthetic apertures for passive imaging have not been reported. There has been considerable activity in the development of sparse array SAIR systems during the past 15 years. These have been aimed at demonstration systems underpinning the development of SAIR systems for aerial surveillance and for Earth observation from low Earth orbit. The challenges faced by both applications are very similar and aerial deployment of Earth observation SAIR demonstrators has been conducted. Earth observation using radio-frequency aperture synthesis is being developed under ESA's MIRAS program⁽⁸⁾ and NASA's ESTAR program⁽⁹⁾ that both operate at 14GHz, although a 37GHz airborne version of the ESTAR system offering 21 milliradian angular resolution is commercially available⁽¹⁰⁾. MIRAS uses a two-dimensional, Y-shaped array of hexagonal antennae whereas ESTAR employs a one-dimensional array of stick antennae that is push-broom scanned to form a two-dimensional image. Other candidate techniques are the closely related RadSAR⁽¹¹⁾ and supersynthesis⁽¹²⁾ techniques, the Mills Cross⁽¹³⁾ and hybrid techniques combining a mechanical scan with one- and two-dimensional aperture synthesis⁽¹⁴⁾. A real-time hybrid technique employing real and synthetic apertures has also been demonstrated by ThermoTrex using sparse linear arrays of frequency-scanned antennae⁽¹⁵⁾. Implementation of passive mm-wave SAIR is considerably less mature than conventional passive mm-wave imaging and this is manifest in the specifications of the instruments: whilst the ThermoTrex hybrid SAIR forms a real-time 60 \times 74 pixel image with a radiometric sensitivity of 5K, the mechanically scanned QinetiQ MERIT imager forms an image at a similar frame rate and slightly larger pixel count with a higher sensitivity of 1K.

Aperture synthesis offers the potential for real-time PMI from antenna arrays that can be two dimensional or even conformal to the structure of a military vehicle. The basic concept, as depicted in Fig. 2, is to integrate an array of n antennae into the structure of the UAV

so that an antenna is synthesised with a resolution similar to that of a filled antenna with the length and breadth of the UAV. The noise-like mm-wave signal from each antenna is correlated with the signal from each and every other antenna in $n(n-1)/2$ complex correlators to form a set of complex visibilities which are used to calculate the mm-wave image using a Fourier-transform relationship. Loosely speaking, this Fourier transform is analogous to that applied by the lens or reflector of a conventional imager, but is applied by computer algorithms rather than by focusing. It can be appreciated that the complexity of such a system is greater than for a conventional imager. If useful target detection performance is to be achieved from a SAIR that can be built at an acceptable cost, careful consideration of the design parameters is required. We propose here a top-level design for such a system.

The most important SAIR parameters include radiometric temperature sensitivity, field of view and complexity. In general the first two parameters can only be improved with a cost and complexity penalty. Previous approaches to SAIR have not addressed the specific restrictions that apply to deployment from small aircraft such as UAVs. For remote sensing from a satellite it is possible to achieve a very good ratio of sensitivity to complexity using one-dimensional aperture synthesis with a fan beam⁽¹⁶⁾ similar to that proposed by the ESTAR program. However, this requires an antenna array that is incompatible with deployment on an aircraft and we describe here alternative approaches. Several techniques have been considered⁽¹⁷⁾ and the techniques that have received most attention here are variations on two-dimensional aperture synthesis. This offers the essential feature of real-time calibration of an antenna array that flexes with the UAV structure. The main challenge remaining is to achieve useful performance with acceptable complexity and cost.

To implement passive mm-wave imaging from a SAIR mounted on a UAV platform, the following challenges must be addressed:

- The antenna pattern of the SAIR must be well behaved.
- Sensitivity must be adequate.
- It must be possible to calibrate the antenna array in real time.
- It must be possible to integrate the antenna array and signal harness into the UAV structure without adversely effecting its aerodynamics and function.
- The SAIR should ideally have electromagnetic compatibility with the data link and other sensors, such as SAR.

We have calculated the antenna patterns that can ideally be achieved with an array of antennae mounted onto the real estate that appears to be available on a range of UAVs and it generally appears that antenna patterns can be formed that have acceptable sidelobe levels and a narrow main beam. In the case of a small UAV, such as Phoenix, the achievable angular resolutions are comparable to that of a current wide field-of-view thermal imager. An operational centre frequency of 80GHz has been assumed since this offers the good foul-weather scene contrast and the possibility of exploiting low-cost commercial off-the-shelf radio-frequency components developed for the automotive radar market.

Three approaches to deployment of a SAIR on a UAV were identified as the most promising. With reference to Fig. 3 which depicts the antennae mounted on the UAV real estate and the associated, instantaneous ground footprint, these are:

1. Wide field-of-view across-track imaging, with narrow along-track field of view using a filled regular array of narrow stick antennae across the wings and along the fuselage. The antennae are aligned with the fuselage and the array shape is approximately a 'T' or a cross. There are no aliases in the across-track direction, but there are aliases in the along track dimension.
2. As above, except the stick antennae are wide, so that the field of view is narrowed in the across-track dimension. In principle the antennae may be electronically scanned across the field of regard of the swath width.

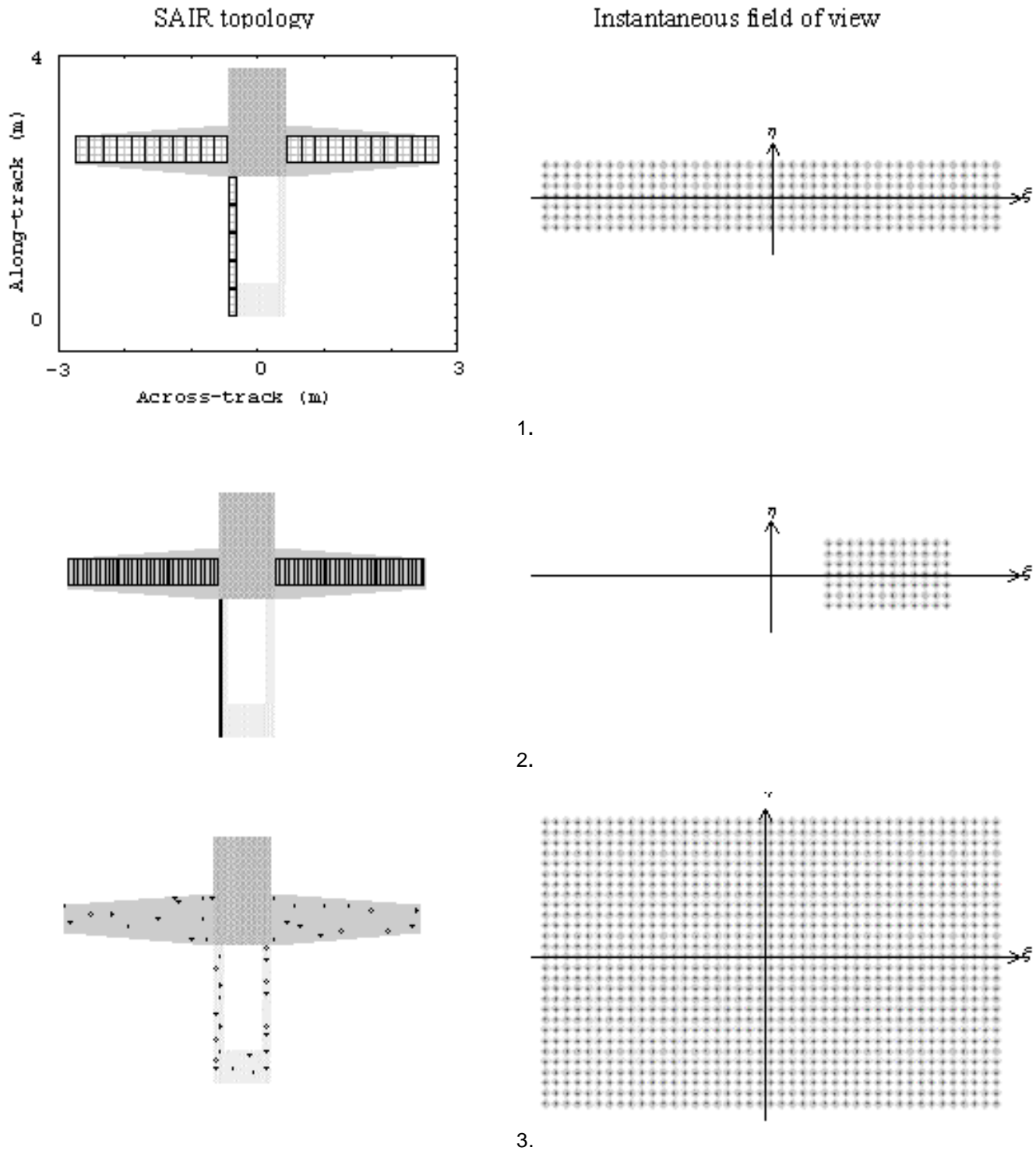


Figure 3. Depiction of antenna arrays and fields of view of the three aperture synthesis methods considered: 1. wide field of view across-track imaging with a regular array, 2. narrow field of view across-track imaging with a regular array and 3. wide field of view imaging with an irregularly-spaced array of antennas.

3. Wide field-of-view imaging using irregular arrays of small feed-horn antennae with sparse, irregular sampling of the spatial frequencies in the scene.

In Section 2 we discuss the antenna pattern that can be achieved from the available real estate on a typical UAV and how closely this

might be approached by the candidate SAIR techniques. In Section 3, we describe the calculation of the radiometric sensitivity and in Section 4 we present system-level calculations of important parameters for each of the three SAIR techniques outlined above. In Section 5 we discuss how the SAIR may be calibrated and conclusions are presented in Section 6.

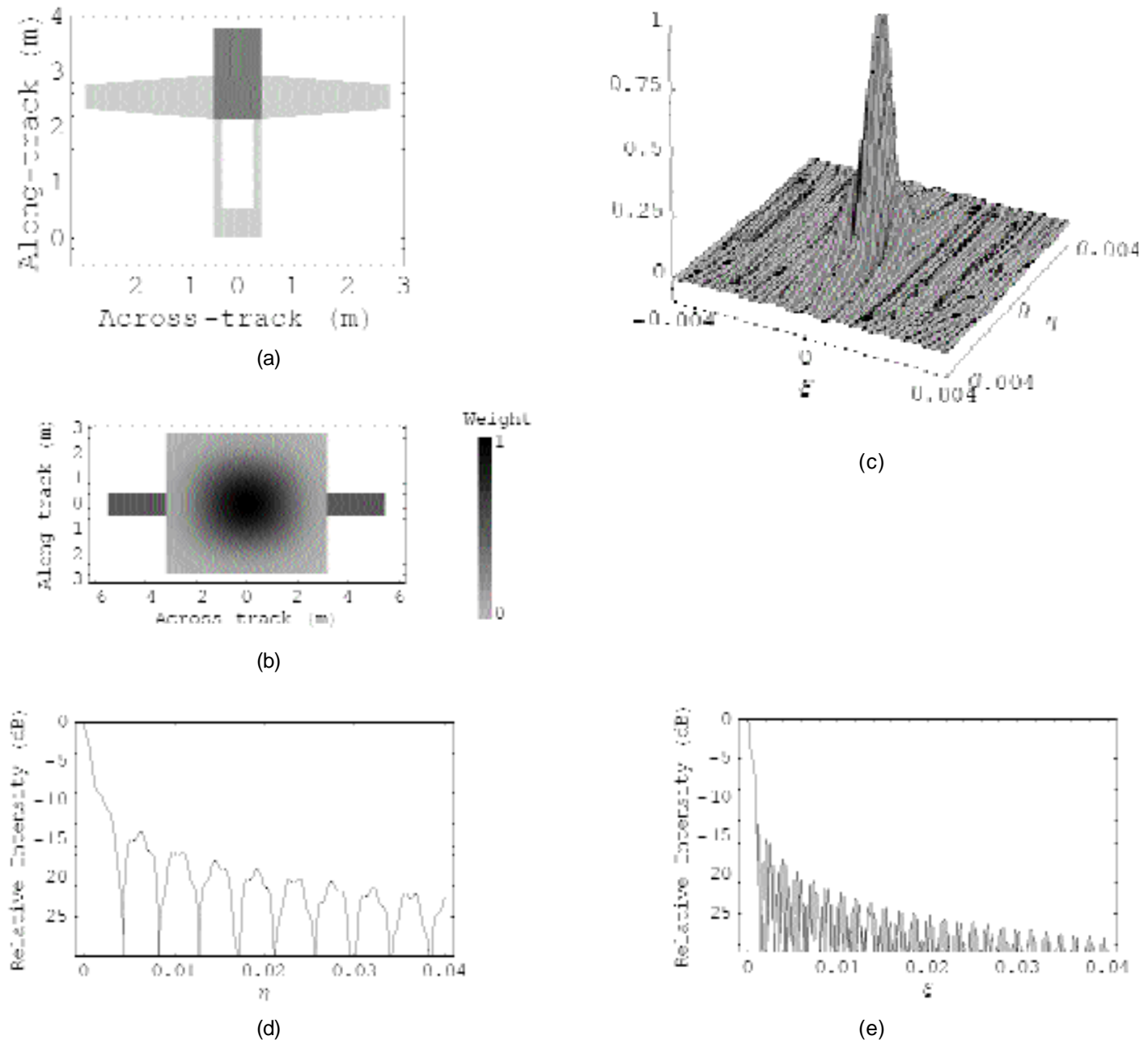


Figure 4. (a) Available real estate for mounting antennae, (b) weighted support region for this array, (c), (d) and (e) antenna patterns obtainable from this support region.

2.0 ANTENNA PATTERN

The antenna pattern of an imager can be calculated from the Fourier transform of the autocorrelation of the antenna aperture amplitude distribution. That is, to say that the amplitudes of the scene spatial frequencies sampled by the imager are obtained from the autocorrelation function. For a filled aperture, the autocorrelation function has a smoothly varying normalized value between zero and one, whereas for a sparse synthetic aperture array with zero redundancy (that is, all antenna vector separations occur only once) the only values that occur are zero and one. This tends to result in a square law relationship between the two antenna patterns. For example, for a uniformly weighted filled antenna the autocorrelation function is a triangle function and the antenna pattern is a $sinc^2$ function, whereas for a sparse antenna array, the autocorrelation function is a $Rect$ function and the antenna pattern is a sinc function. At first glance it appears that the

power of two for the filled dish will result in a narrower antenna pattern with lower sidelobes than for the sparse antenna array, but in practice the Hermitian nature of the measured quantities (the complex spatial frequencies of the scene) enables the effective dimension of the aperture to be doubled and the use of an appropriate weighting function in the image reconstruction enables the sidelobes to be suppressed. These factors cancel, so that the beam width and sidelobe level of a sparse array can be equal to those of a filled array.

The autocorrelation function represents the set of vector spacings of all the antennae in the antenna array and is plotted here in a region referred to as the support region. For a filled aperture, the support region is a continuous function. When an antenna array is employed, the support region is sampled at a set of points represented by the set of vector spacings of the antennae in the synthetic aperture array. This can be illustrated by reference to Fig. 4. The outline of a small UAV is

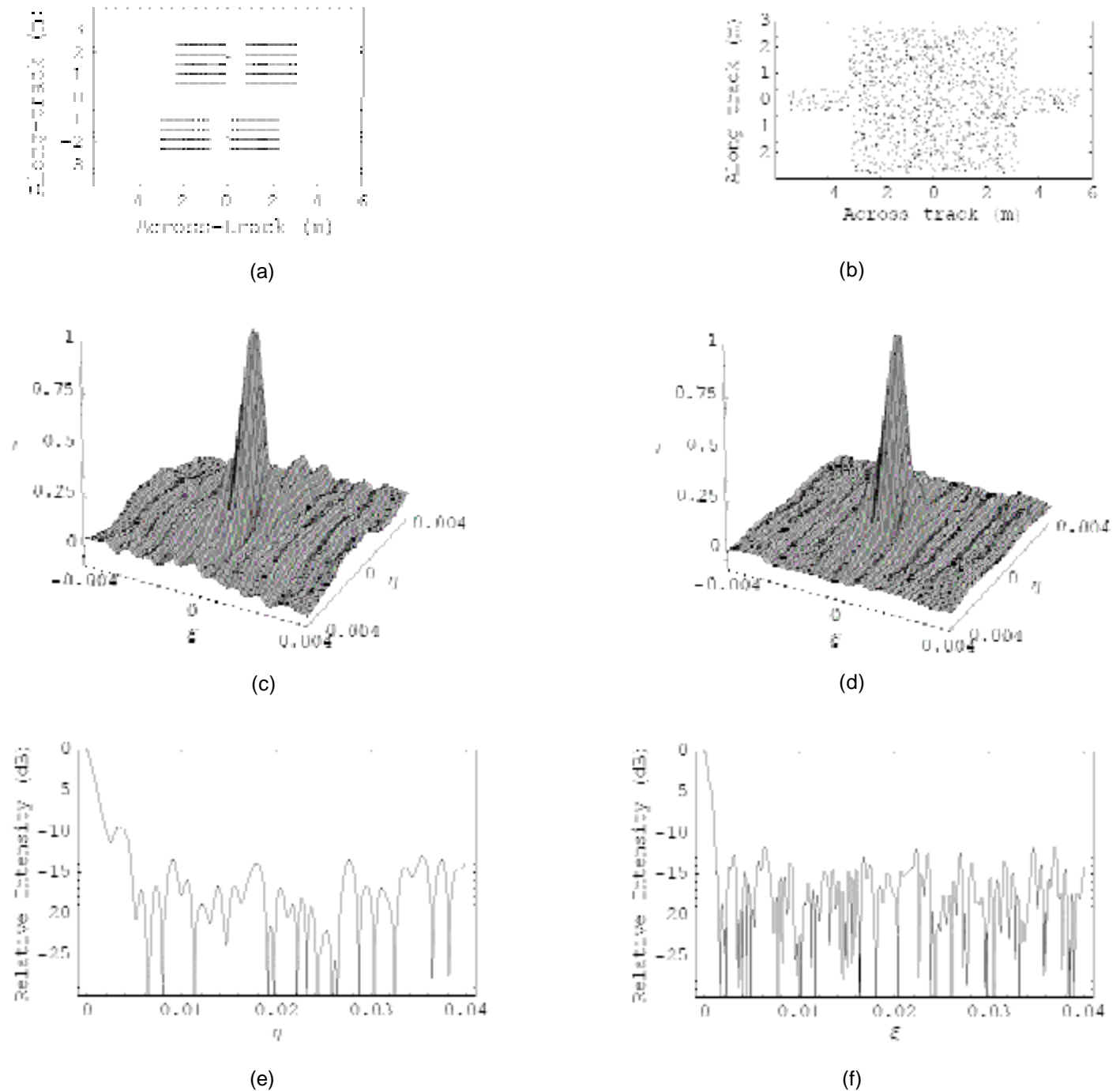


Figure 5. (a) Sampling of support region for method 1, (b) irregular sampling of support region with method 3 (c)SAIR antenna response with method 3 and 1,000 samples in the support region and (d) 10,000 samples in the support region, (e) and (f) are slices along the principle axes through (c).

shown in Fig. 4(a), where the available mounting surfaces for antennae are shaded light grey. The support region for the filled antenna array is shown in Fig. 4(b) and the calculated antenna pattern is shown in Fig. 4(c) as a two dimensional plot and in (d) and (e) as sections along the ξ and η axes, where ξ and η are direction cosines parallel and perpendicular to the UAV fuselage. The weighting of the antenna support region is indicated in (b) and is given here by a Hamming weighting for the main rectangle of the support region and a constant level of 0.5 for the smaller rectangles. The optimum weighting function may be derived from a consideration of accept-

able sidelobe levels and width of the main lobe, although no rigorous optimisation has been applied here.

Each complex correlator in the SAIR yields measurements in the support region which enable calculation of one complex angular frequency component of the scene intensity distribution. Nyquist sampling of the scene spatial frequencies is achieved by sampling the support region at $\lambda/2$ intervals and this will yield an antenna pattern that is almost identical to that of a filled antenna as shown in Fig. 4(d) and (e). Approximately 8,000,000 correlators would be required to fully sample this support region. The inputs to these

correlators could be generated by a sparse array of small antennae. For n antennae, there are $n(n - 1)/2$ possible combinations so approximately 4,000 antennae and receivers will be required. This number of antennae and correlators is considered prohibitively complex and some simplification is required. This was the prime motive for proposing the three SAIR techniques mentioned in Section 1.

The first of these three techniques mentioned in Section 1 involves Nyquist sampling of the support region in the across-track dimension and sub-Nyquist sampling in the along-track dimension. This inevitably introduces aliases (also known as grating lobes) in this dimension that restrict the field of view to about one half of the antenna pattern width in that direction. The second technique involves sub-Nyquist sampling in both directions and results in aliases in both directions. The third technique uses irregular sampling of the support region. This produces no aliases and the sidelobes are noise-like and uniformly distributed across the image. As will be seen, it appears to be possible to design a SAIR with irregular sampling of the support region that enables an acceptable antenna pattern to be obtained from a less complex system, with improved radiometric sensitivity. The normalized RMS sidelobe level is approximately equal to the square root of the number of independent samples in the support region. For n antennae there are $n(n-1)/2$ independent points in the support region, so for large n , the RMS sidelobe level is approximately equal to $\sqrt{2/n}$.

These points are illustrated in Fig. 5. Figure 5(a) and (b) show sampling of the support region using methods 1 and 3. It can be appreciated from comparison of Fig. 4(a) and Fig. 5(a) that there is a high degree of redundancy for vector spacings of the antenna array across the wings, but zero redundancy elsewhere. The reduction in sidelobe levels can be seen from comparison of Fig. 5(c), which used 1,000 samples in the support region and Fig. 5(d), which used 10,000 samples. One-dimensional sections along the principal axes of Fig. 5(c) are shown in Fig. 5(e) and (f). It might be noted that a SAIR antenna pattern has both negative and positive sidelobes, unlike the power patterns obtained from real apertures, which are always positive. In Figure 5(e) and (f), the modulus of the antenna pattern has been taken. The full width at half maximum (FWHM) widths of the antenna patterns are $\theta_x = 0.0007 \approx 0.04^\circ$ across track and $\theta_y = 0.0014 \approx 0.08^\circ$ along track for all antenna patterns.

The design of the antenna array that gives irregular but statistically uniform coverage of the support region is not straight forward. Uniformly distributing antennae over the available mounting area on the UAV will result in a support region that is more densely sampled close to the origin. One approach to designing the antenna array may be to use optimisation techniques to optimize the antenna array topology and other parameters using an appropriate cost function, such as SAIR antenna pattern.

3.0 RADIOMETRIC SENSITIVITY

The radiometric sensitivity of a synthetic aperture radiometer is quoted in several forms that need to be carefully interpreted to give a consistent meaning. The general starting point in deriving radiometric sensitivity, ΔT , is to derive the variance on a measurement of the fringe visibility. In synthesising the image from the visibility functions, the variances accumulate in each pixel to give an increased variance in the apparent temperature in each pixel. The resulting standard deviations are scene dependent and a good approximation to a representative value of ΔT is obtained by assuming that the scene is unstructured and the measured visibilities are low. The radiometric sensitivity of a SAIR can then be written as (see appendix)

$$\Delta T \approx \sqrt{\frac{1}{n}} \sqrt{\frac{1}{B}} \sqrt{\frac{1}{h}} \sqrt{\frac{1}{v}} \sqrt{\frac{1}{\theta_x}} \sqrt{\frac{1}{\theta_y}} \sqrt{\frac{1}{w_{rms}}} \dots (1)$$

where T_B is the average scene temperature within the field of view of the antenna elements, T_A is the amplifier noise temperature, N is the total number of baselines, r_i is the redundancy of the i th baseline, B is the radio-frequency bandwidth of the SAIR, τ is the integration time and w_{rms} is the root-mean-square value of the function used to weight the visibility measurements prior to calculation of the image from their Fourier transformation. This expression is a simplification of a more general expression and is true in the limit of an unstructured scene. In effect, each baseline adds more information to the image, but also increases the noise level. The implication is therefore that the minimum number of baselines should be employed in constructing the image. This will mean that the array has zero redundancy or near-zero redundancy so that the summation in Equation (1) is equal to N . Equation (1) is slightly different to that used in radio astronomy where scenes are highly structured and the approximation of low scene contrast is not valid. It should also be noted that the area of the antennae does not appear since it is assumed that the field of view is completely filled by the Earth. The power at the output terminals of each antenna element (and consequently the variance in the measured visibilities) is therefore independent of the effective areas of the antenna elements.

It can be seen from Equation (1) that for lowest ΔT and a non-redundant array, the number of baselines should be the smallest number that is compatible with acceptable image quality. This is the reason why sparse sampling of the support region enables lower values of ΔT to be attained than full or denser sampling. The challenge then is to seek the value of N that gives the desired optimum trade off of image quality against sensitivity. This general expression can be used to calculate directly ΔT for all three SAIR techniques described here where the summation and the integration time are determined by parameters of the array and the UAV. This expression is used directly for calculation of the sensitivity of the irregular array (SAIR technique 3), but for the use of regular arrays (techniques 1 and 2), some further simplification is enlightening. In the Appendix it is shown that Equation (1) can then be simplified to give

$$\Delta T \approx \sqrt{\frac{1}{n}} \sqrt{\frac{1}{B}} \sqrt{\frac{1}{h}} \sqrt{\frac{1}{v}} \sqrt{\frac{1}{\theta_x}} \sqrt{\frac{1}{\theta_y}} \sqrt{\frac{1}{w_{rms}}} \dots (2)$$

where n is the total number of antennae, θ_x and θ_y are the angular resolutions in the across-track and along-track directions, λ_x and λ_y are the antenna spacings (in units of a half wavelength) in the across-track and along-track dimensions, B is the frequency bandwidth of the radio-frequency receivers, v is the speed of the platform and h is its height. To enable alias-free imaging in the across-track dimension, we will employ $\lambda_x = 1$. It is also implied by Equation (2) that to minimise ΔT for a given number, n , of receivers and antennae, the antenna spacing in the along-track direction should be as great as possible. When the antenna spacing is greater than $\lambda/2$ (that is, $\lambda_y > 1$), aliased images will be introduced. This means that only those pixels closest to $\lambda = 0$ offer low contamination from aliases and the effective integration time is reduced. In practice, this results in a halving of the effective integration time and an increase of ΔT by a factor of $\sqrt{2}$. This entails a trade off of a reduction in the number of expensive receivers for an increase in the number of correlators — a trade off that will reduce the overall system cost and complexity.

In practice, one may be more interested in detecting small objects and improved performance will then be achieved by configuring the antenna array such that there are proportionately more long baselines and fewer short baselines. This could be achieved by having proportionately greater numbers of antennae towards the ends of the wings of a UAV than the centres. This would result in improved sensitivity at high spatial frequencies and improved detection of small objects. The radiometric sensitivity denoted by Equation (2) should therefore be taken as just an approximate guide to performance.

As can be seen from Equation (2), improvements in sensitivity can be bought at the expense of increased receiver bandwidth B ,

Table 1
Salient parameters for UV-mounted SAIRS

Technique	Small UAV			Large UAV		
	1	2	3	1	2	3
Antenna length	0.44	0.44	0.003	0.36	0.36	0.003
Antenna width	0.002	0.1075	0.003	0.002	0.1075	0.003
Total number of antennae	1,862	47	46	5,962	158	46
Total number of full-band complex correlations	16,220	331	1,000	63,521	1,489	1,000
Maximum single-channel bandwidth (MHz)	63	3,123	63	23	1,160	23
Radiometric sensitivity — no channelisation, maximum integration time (K)	7.6	1.4	0.18	18.0	1.9	0.22
Radiometric sensitivity — no channelisation, snapshot integration time (K)			5.1			7.4
Swath width at Nadir	±60°	±2°	±60°	±60°	±2°	±60°

increased numbers of antennae, n , and improved receiver noise, T_A . The latter is probably the least important parameter to be traded: improvements in sensitivity are marginal for reductions in amplifier noise below the background noise temperature of 300K. In the medium-to long-term future, the costs of the antennae/receivers in mm-wave aperture synthesis imaging are likely to considerably exceed the costs of the digital correlation hardware. This is an even more important consideration for deployment on a UAV where integration of antennae into the aircraft superstructure places an additional technical difficulty and cost penalty that makes it desirable to minimise their number. It is assumed here that the maximum possible feasible bandwidth will be employed and the minimum number of antennae.

It can be seen from Equation (2) that the radiometric sensitivity improves with the square root of the bandwidth, B , of the intermediate frequency (IF). The scale of the synthesized image is proportional to frequency and this limits the maximum instantaneous bandwidth to that which does not introduce noticeable blurring of the image. This is equivalent to stating that temporal coherence must be maintained across the array, which requires the following condition to be satisfied:

$$B_{\max} \geq \frac{c}{D \sin \theta_{\max}} \quad \dots (3)$$

Where c is the speed of light, D is the width of the SAIR aperture and θ_{\max} is the maximum angle with respect to the centre of the field of view. If greater bandwidths are required so as to yield improved radiometric sensitivity, then the full IF bandwidth must be channelised into frequency bands with bandwidths less than B_{\max} .

4.0 DESIGN PARAMETERS FOR SAIR TECHNIQUES

In this section we report estimates of parameters for SAIRS designed by each of the three techniques and these are summarised in Table 1. Results are presented for two representative UAVs denoted here as simply 'small UAV' and 'large UAV'. The outline of the small UAV is shown in Fig. 4(a) and has a wing span of 5.5m. The larger UAV has a wing span of 14.8 m. They are assumed to be flying at 2,000m and 6,000m respectively. The techniques outlined in Section 2 are denoted by numbers 1, 2 and 3. The dimensions of the antenna elements assumed for each technique are indicated in rows three and four together with the total numbers of antennae required for sampling of the support regions. We have shown that for 1,000

sample points in the support region the central lobe of the antenna pattern is close to the optimum that can be achieved and this gives the required high angular resolution. However, thinning of the antenna array results in an increased fraction of energy in the side-lobes and this leads to an increase in the fixed-pattern noise in the image. The reduction of this fixed pattern noise is an area of ongoing research. Methods include deconvolution, system trade-offs and multi-parameter optimisation of the antenna pattern. The maximum unchannelised bandwidths are determined by the field of view and the width of the antenna array and are given in the seventh row. The calculated radiometric sensitivities are shown in the eighth row under the assumption that the maximum possible integration time can be used. This requires pixel averaging. This will be less than perfect and so radiometric sensitivities will actually be somewhat worse than these values. For snapshot imaging, the integration time is somewhat shorter and the resulting sensitivity is shown in row 9 for method 3.

The most significant aspect of the results is that technique 3, which uses an irregular array, enables wide field of view imaging and offers higher sensitivities whilst requiring much lower complexity (in terms of number of correlators, number of antennae/receivers and required bandwidth). However, sensitivities of 1-2K are desirable for most passive mm-wave imaging tasks and so the predicted values of about 5K and 7K for snapshot imaging are inadequate. Sensitivity improves in proportion to $1/\sqrt{B}$, so an increase by a factor of about 16 in B will enable these target sensitivities to be attained. The lowest cost route to improving B is by pixel averaging to increase θ . However channelising a wider bandwidth into contiguous bands so as to increase B is also possible and this also promises to reduce sidelobe levels by smearing of the images.

A particularly important parameter is the small number of antennae and receivers required by technique 3. Not only does this reduce cost, but also the integration of the required antennae into the UAV structure is less problematic than for the other methods and the aggregate weight of antennae and receivers is reduced. The total weight of the SAIR is of particular importance for deployment on small air vehicles such as a UAV that have limited a payload capacity. For a small UAV such as that considered here the maximum payload is typically 50kg. The total weight of the SAIR system will be dominated by the aggregate weight of antennae receivers and signal harness (that is, the waveguides used to transmit the radio-frequency signal from each antenna to the correlators). This weight increases approximately linearly with the number of antennae and this is another reason for favouring technique 3, which uses the lowest number of receivers. From Table 1 it can be seen that using technique 3, the SAIR for the small UAV requires 46

antennae. The use of VLSI (very large scale integration) technology for the correlator units means that their contribution to the overall weight will be small, so that the average weight of each antenna, receiver and associated signal harness should be less than 1kg. This is readily achievable using conventional microwave components, printed circuit antennae and low-loss coaxial cable for signal harness. The use of optical transmission of radio-frequency signals⁷ offers potential for further reduction in weight of the signal harness.

5.0 SYSTEM CALIBRATION

Calibration for SAIR systems is considerably more complex than for conventional radiometers and is proving to be one of the greatest obstacles to their deployment. The main difficulties lie in coherently combining complex signals over distances of several metres with accurately known amplitude and phase characteristics. However, calibration for SAIR systems is more tractable than for phased-array radar, since calibration corrections are applied in computer software rather than microwave hardware. Mounting of a SAIR onto a UAV is a particularly demanding problem, since the antennae will be mounted to the aircraft wings and fuselage, which will undergo significant flexing during UAV operation. Further problems are likely to be experienced due to thermal drift in the SAIR components. Calibration of a UAV-mounted SAIR will require the calibration and real-time software correction of all of these factors, where real-time refers to the rate at which parameters, such as the shape of the antenna array, are changing.

The fundamental parameters that are measured by a SAIR are the set of complex visibility functions for each baseline that is available from the antenna array topology. The general principles of calibration of synthetic aperture radiometers have been covered in the literature for MIRAS⁽¹⁸⁻²⁰⁾ and ESTAR⁽²¹⁻²³⁾. For 1K temperature error, the net complex amplitude error in measurement of fringe visibility should be calibrated to within 1% in amplitude and 0.5° in phase^(18,20). It is convenient to consider the calibration of the antenna structure and receivers separately. Phase errors due to the antenna structure accrue due to physical distortion of the array from their nominal positions, but can be corrected by measurement of the array shape and application of a correction factor in software. It is proposed here that the calibration methods proposed for MIRAS using noise injection to overlapping subsets of receivers⁽²⁴⁾ should be applied for periodic re-calibration of the receiver and correlator chain. This calibration is with respect to a baseline calibration performed in the laboratory. The calibration interval should be determined by the scale time for drift in the complex gain of the electronics and the signal distribution system. The antenna array will vibrate and its shape needs to be calibrated in real-time. Shape calibration will enable calibration and image reconstruction using the G-matrix technique developed for ESTAR22⁽²²⁾. The proposed calibration sequence consists of

- Baseline laboratory calibration of the receiver chain using noise injection.
- Baseline laboratory calibration of antenna shape.
- Baseline calibration of the combined antenna/receiver chain complex amplitude response via measurement of antenna-pair impulse responses.
- Periodic in-service re-calibration of the receiver chain with respect to the baseline calibration.
- Real-time calibration of the antenna shape.

Thus calibration consists of baseline calibration followed by in-service re-calibration with respect to this baseline and the receiver and antenna components are calibrated independently.

It is clear from work on both ESTAR and MIRAS that accurate knowledge of antenna patterns is essential for calibration. Recent reports on ESTAR⁽²³⁾ indicate that mutual coupling plays a major

role in determining the antenna pattern but can be accurately described if only the coupling to the nearest neighbour was included. This may also be the case for the irregular arrays proposed here, although the use of omnidirectional antennae rather than stick antennae will greatly reduce mutual coupling and hence reduce its impact on SAIR calibration. With little need for short baselines in surveillance, the mutual coupling in sparse arrays of circular antennae will be smaller than for ESTAR and MIRAS although scattering from the UAV structure and sensor pods may still introduce significant artefacts that will need to be calibrated.

It was noted by Weissman and Le Vine⁽²³⁾, that displacements of antennae of 0.003 l in the plane of the antenna resulted in errors of 3K in the reconstructed image and that curvature of 0.01° along the antenna array introduced similar sized errors. The required 0.5° phase accuracy quoted by Camps et al⁽¹⁸⁾ suggests an accuracy of approaching 0.001 l is required in the plane orthogonal to antenna array. It is proposed that the response patterns of the antenna array can be measured in the laboratory for a given antenna shape. Real-time measurement of antenna shape once in service will then enable calculation of the actual in-service antenna array response patterns. The antenna array will change shape once in service due to flexing of the UAV structure. It is not necessary to stabilise the shape of the wing, only to be able to measure its shape with sufficient accuracy to be able to predict the impulse response of the antenna array associated for the measured shape.

As a working estimate of the antenna calibration accuracy required, we will assume 0.003 l in the plane of the UAV and 0.001 l out of the plane. These are probably a little in excess of the accuracies actually required (for example the lower mutual coupling between antennae will reduce the sensitivity to in-plane movement). These figures correspond to 10µm and 3µm for the 80GHz antenna structure. The most suitable method for measuring the mechanical shape of the array is with electrical or optical-fibre strain gauges. Optical fibre strain sensors based on either Bragg gratings or broadband-light interferometry using a superluminescent LED light source⁽²⁵⁾ can yield high accuracy shape measurement and can be readily integrated into composite structures such as the UAV frame. If necessary a single optical fibre may be used to multiplex many sensors, but as an absolute minimum a single sensor is required for each degree of freedom of a flexible structure⁽²⁶⁾. Traditionally interrogation is achieved with moving-mirror Michelson interferometers, but for use on an aircraft no-moving-parts interferometry using channelled spectrum⁽²⁵⁾ or spatial interferometers⁽²⁷⁾ is more attractive.

Fibre sensors may be imbedded on opposite sides of the wing, and bending may be measured from the differential strain in each fibre. With white light optical interferometry, 1µm displacement can be measured⁽²⁷⁾ so that for a 1m long sensor and a wing 2.75m long and 5cm thick, displacements of less than 0.7µm (worst case) can be measured in the plane of the antenna which is equal to about 0.01° of phase error in the mm-wave signal: an accuracy more than 30 times better than is required for accurate calibration. In summary, it is proposed that periodic in-service receiver calibration follows calibration techniques already developed for MIRAS, but real-time calibration of the antenna patterns will also be required. This can be achieved using the G-matrix method developed for ESTAR, but with the addition of real-time measurement of antenna array shape that enables real-time calculation of the antenna-pair impulse response.

6.0 CONCLUSIONS

We have shown that it is possible, in principle, to integrate an antenna array into the structure of a UAV and use aperture synthesis methods to form a passive mm-wave image of a scene centred on nadir. The results presented indicate that a specific level of performance is attainable for a given, acceptable level of complexity in the SAIR system. A modest improvement in this performance is desirable and there are several approaches to improve the balance of

image quality against SAIR complexity, including deconvolution methods, and multi-parameter optimisation of the antenna pattern. These are the subjects of on-going research. Calibration of a SAIR mounted into a flexible structure such as a UAV will be difficult, but given the algorithms and optical fibre shape measurement technology that exists, calibration appears to be a tractable problem. The technique shows promise for passive imaging of scenes through foul weather and obscurants from small air-borne platforms.

ACKNOWLEDGEMENT

This work was funded under an extra mural research contract from QinetiQ, Malvern, UK.

REFERENCES

1. Quote from US secretary of defense William S. Cohen, 14 October 1999.
2. *IEEE Transactions on Geoscience and Remote Sensing*, special edition, 1998, **36**.
3. SKOU, N. and LAURSEN, B. Measurement of ocean wind vector by an airborne, imaging polarimetric radiometer, *Radio Science*, 1998, **33**, (3), pp 669-675.
4. APPELBY, R., ANDERTON, R.N., PRICE, S., SALMON, N.A., SNCLAIR, G.N, BORRILL, J.R., COWARD, P.R., PAPAOKOSTA, P., LETTINGTON, A.H. and ROBERTSON, D.A. Compact real-time (video rate) passive millimetre-wave imager, 1999, Conference on passive millimetre-wave imaging technology, SPIE 3703, pp 13-19.
5. MOFFA, P., YUJRI, L., JORDAN, K., GIU, R.S., AGRAVANTE, H. and FORNACA, S. Passive millimetre wave camera flight tests, 2000, Conference on passive millimeter-wave imaging technology, SPIE 4032, pp 14-21.
6. HARVEY, A.R., APPELBY, R., COWARD, P., GREENAWAY, A.H., ANDERTON, R. and HAWKINS, G. Electronic beam-steering for passive millimetre-wave imaging, 1998, Fourth int Conf on mm and submm-waves and applications, San Diego, 20-23 July, SPIE 3465.
7. BLANCHARD, P.M., GREENAWAY, A.H., HARVEY, A.R. and WEBSTER, K. Coherent optical beamforming with passive millimetre wave arrays, 1999, *J Lightwave Tech*, **17**, (3), pp 418-425.
8. MARTIN-NEIRA, M., GOUTOULE, J.M., KNIGHT, A., CLAUDE, J., BARA, J., CAMPS, A., TORRES, F., CORBELLA, I., LANNES, A., ANTERRIEU, E., LAURSEN, B. and SKOU, N. Integration of MIRAS breadboard and future activities, 1996, IGARSS, pp 869-871.
9. LE VINE, D.M., GRIFFIS, A.J., SWIFT, C.T. and JACKSON, T.J. ESTAR: A synthetic aperture microwave radiometer for remote sensing applications, 1994, *IEEE* **82**, **12**, pp 1787-1801.
10. *ESTAR 37 Airborne Imaging Radiometer System*, Publicity material, Quadrant Engineering, Amherst, MA, USA.
11. EDELSON, C. Applications of synthetic aperture radiometry, 1994, IGARSS, pp 1326-1328.
12. KOMIYAMA, K. Indoor experiment of two-dimensional supersynthesis radiometer, 1994, IGARSS, pp 1329-1331.
13. MAILLOT, H.A. A cross beam interferometer for high resolution microwave sensing, 1993, *IEEE Aerospace Appl Conf*, pp 77-86.
14. MARTIN-NEIRA, M. and FONT-ROSSELLO, J. Mechanically scanned interferometric microwave radiometer using sub-arraying, October 1997, ESTEC Internal Report, XR1/108.97/MMN.
15. MARTIN, C.A., LOVBERG, J.A., CLARK, S.E. and GALLIANO, J.A. Real-time passive millimetre-wave imaging from a helicopter platform, 2000, *Passive millimetre-wave imaging technology IV*, SPIE 4032.
16. HARVEY, A.R., GREENAWAY, A.H., CAMPS, A., CORBELLA, I., TORRES, F., BARA, J. and MARTIN-NEIRA, M. Millimetre-wave aperture synthesis radiometry for snow and ice mapping, 1999, *Int Conf on Geoscience Remote Sensing*, Hamburg, 28 June-2 July 1999.
17. HARVEY, A.R. Report on passive aperture synthetic mm-wave imaging from unmanned airborne vehicles, October 1999, Report to DERA DAPS/AH/42/99/0.A.
18. CAMPS, A., BARA, J., TORRES, F., CORBELLA, I. and ROMEU, J. Impact of antenna errors on the radiometric accuracy of large aperture synthesis radiometer, 1997, *Radio Science*, **32**, (2), pp 657-668.
19. TORRES, F., CAMPS, A., BARA, J., CORBELLO, I. and FERRERO, R. On-board phase and modulus calibration of large aperture synthesis radiometers: study applied to MIRAS, *IEEE Transactions on Geoscience and Remote Sensing*, 1996, **34**, (4), pp 1000-1009.

20. TORRES, F., CAMPS, A., BAR, J. and CORBELLA, I. Impact of receiver errors on the radiometric accuracy of large aperture synthesis radiometer, *Radio Science*, 1997, **32**, (2), pp 629-641.
21. RUF, C.S. Error analysis of image reconstruction by a synthetic aperture interferometric radiometer, *Radio Science*, 1996, **26**, (6), pp 1419-1434.
22. TANNER, A.B. and SWIFT, C.T. Calibration of a synthetic aperture radiometer, *IEEE Transactions on Geoscience and Remote Sensing*, 1993, **31**, (1), pp 257-267.
23. WEISSMAN, D.E. and LE VINE, D.M. The role of mutual coupling in the performance of synthetic aperture arrays, *Radio Science*, 1998, **33**, (3), pp 767-779.
24. TORRES, F., CAMPS, A., BARA, J., CORBELLA, I. and FERRERO, R. On-board phase and modulus calibration of large aperture synthesis radiometers: study applied to MIRAS, *IEEE Transactions on Geoscience and Remote Sensing*, 1996, **34**, (4), pp 1000-1009.
25. BURNETT, J.G., ERRY, G.R.G., DICKSON, R., MCBRIDE, R., GANDER, M., JONES, J.D.C., BLANCHARD, P.M., GREENAWAY, A.H. and HARVEY, A.R. Channelled spectrum interrogation of an all fibre broadband interferometric differential strain sensor, 1998, *European Workshop on Optical Fibre Sensors*, 3483, Ch 66, pp 174-178.
26. WOODS, S., GREENAWAY, A.H. and HARVEY, A.R. Optimal shape reconstruction using modal decomposition, 1998, *IOP conference on applied optics and electronics*, Brighton, UK, 16-19 March, pp 145-150.
27. HARVEY, A.R. Determination of the optical constants of thin films in the visible by dispersive Fourier transform spectroscopy, *Review of Scientific Instruments*, 1998, **69**, (10), pp 3649-3658.
28. RUF, C.S., SWIFT, C.T., TANNER, A.B. and LE VINE, D.M. Interferometric synthetic aperture radiometry for the remote sensing of the Earth, *IEEE Transactions on Geoscience and Remote Sensing*, 1988, **26**, (5), pp 597-611.
29. THOMPSON, A.R., MORAN, J.M. and SWENSON, G.W. *Interferometry and Synthesis in Radio Astronomy*, 1986, Wiley, pp 162-165.

Appendix

In this section we derive expressions for the radiometric sensitivity of SAIR systems mounted to a UAV. The radiometric sensitivity may be written as⁽²⁸⁾

$$T_A \left(\frac{1}{N} \sum_{i=1}^N \frac{1}{r_i} \right) \dots \quad (A1)$$

where T_B is the average scene temperature within the field of view of the antenna elements, T_A is the amplifier noise temperature, N is the total number of baselines and r_i is the redundancy of the i th baseline. Modification of Equation (A1) is required to account for the weighting of the visibility samples. Weighting (also known as apodisation or tapering) is necessary for low sidelobe levels. If a set of weights w_n are applied to the measured visibilities then for a single unresolved source (for which all visibilities are high), the intensity of its image must be scaled by a factor $1/w_{mean}$ where

$$w_{mean} = \frac{1}{N} \sum_{i=1}^N w_i \quad \dots \quad (A2)$$

and the expression for the sensitivity (which can be derived by setting the signal-to-noise ratio to unity) must be multiplied by a factor w_{rms}/w_{mean} ⁽²⁹⁾ where

$$w_{rms} = \sqrt{\frac{1}{N} \sum_{i=1}^N w_i^2} \quad \dots \quad (A3)$$

However, for terrestrial observation, the images are broad and unstructured so that only very short baselines have high visibilities. For all conventional weighting schemes the weighting of these short-baseline visibilities will be very close to unity and so the sensitivity

should be multiplied by a factor w_{rms} so that in place of Equation (A1) the sensitivity is given by

$$S_T = T_B T_A \frac{1}{B} \frac{1}{\sqrt{2}} w_{rms} \dots (A4)$$

which is the expression used for sensitivity for all subsequent calculations. For uniform weighting $w_{rms} = 1$ and for Hamming weighting, as used for the modelling described in this article $w_{rms} = 0.63$. This expression is used directly for calculation of the sensitivity of the irregular array (SAIR technique 3), but for the use of regular arrays (techniques 1 and 2), some further simplification is enlightening.

For maximum sensitivity, the integration time t should be as long as possible. The maximum possible value is the duration that a point on the ground remains within the field of view of a single antenna. For a SAIR mounted to a UAV this is equal to the along-track dimension of the synthesised image divided by the platform speed, which is

$$t = \frac{N_y h}{v} \dots (A5)$$

where N_y is the number of pixels formed along the direction of travel, θ is the FWHM angular resolution in the same direction, h is the height of the platform and v is the speed. The full exploitation of this integration time will require pixel averaging and the tracking of pixels through the synthesised image during the time t . In practice this will be difficult to efficiently achieve, but equation (A6), serves as an upper bound on integration time. A lower bound is the duration for which a point on the ground remains within a resolution cell within the synthesized image and this can be considered the integration time for true snapshot imaging.

Substituting Equation (A5) into equation (A4) and assuming that the antenna array is configured on a rectangular matrix so that there are $N_x N_y$ baselines gives

$$S_T = T_B T_A \frac{1}{BN_y} \frac{1}{\sqrt{2}} w_{rms} \dots (A6)$$

Sensitivity can be improved by introducing redundancy into the processing. This means that more baselines are formed than are required for acceptable image quality, so that averaging of measured visibilities (which are proportional to Fourier image components) results in reduced noise. This is most efficiently achieved by equally spreading the degree of redundancy over all baselines. Equation (A6) can then be written as

$$S_T = T_B T_A \frac{1}{B} \frac{1}{\sqrt{2}} w_{rms} \dots (A7)$$

where we have made the approximation $\theta \approx \lambda/B$; that is, the angular resolution expressed in radians is approximately equal to the angular resolution in cosine vector space. From this equation, we see that the pixel averaging afforded by the push-broom scan means that the sensitivity is independent of the number of pixels in the along-track direction (and hence of the number of antennae in the along track dimension). In practice, it may not be possible for pixel averaging to fully achieve the improvement in SNR that is in principle possible. In the interests of economy, the number of antennae in this direction can therefore be kept as small as possible without adversely affecting sensitivity.

Now, for an antenna array on a spacing of $2\lambda_x/2, 2\lambda_y/2$ where λ_x, λ_y are integers, we have $N_x = 1/\lambda_x, N_y = 1/\lambda_y$ and so we can write, for equal redundancy γ in each baseline,

$$S_T = T_B T_A \frac{1}{B} \frac{1}{\sqrt{2}} w_{rms} \dots (A8)$$

The average redundancy per baseline is given by

$$\gamma = \frac{n(n-1)}{N_x N_y} \dots (A9)$$

so the sensitivity may be written as

$$S_T = T_B T_A \frac{1}{n} \frac{1}{\sqrt{2}} w_{rms} \dots (A10)$$

